Journal of
Composites Science

MDPI

Article

Hydroxyapatite-Based Magnetic Bionanocomposite as Pharmaceuticals Carriers in Chitosan Scaffolds

Anderson Valério Chaves [1], Rafael Melo Freire [2,3], Victor Pinheiro Feitosa [4], Nágila Maria Pontes Silva Ricardo [5], Juliano Casagrande Denardin [6], Davino Machado Andrade Neto [1,7] and Pierre Basílio Almeida Fechine [1,*]

1 Group of Chemistry of Advanced Materials (GQMAT)—Department of Analytical Chemistry and Physical-Chemistry, Universidade Federal do Ceará, Fortaleza, CE 60471-970, Brazil; valerio.anderson@hotmail.com (A.V.C.); davinomachado@gmail.com (D.M.A.N.)
2 Center for the Development of Nanoscience and Nanotechnology, CEDENNA, Santiago 9170124, Chile; rafael.melo@uautonoma.cl
3 Instituto de Ciencias Químicas Aplicadas, Universidad Autónoma de Chile, Santiago 8910060, Chile
4 Paulo Picanço School of Dentistry, Fortaleza, CE 06803-440, Brazil; victorpfeitosa@hotmail.com
5 Laboratory of Polymers and Materials Innovation (LPIM)—Department of Organic and Inorganic Chemistry, Universidade Federal do Ceará—UFC, Fortaleza, CE 60451-970, Brazil; naricard@ufc.br
6 Departamento de Física, Universidad de Santiago de Chile, Santiago 9170124, Chile; jcdenardin@gmail.com
7 Federal Institute of Education, Science and Technology of Ceará—Campus Camocim, Camocim, CE 62400-000, Brazil
* Correspondence: fechine@ufc.br; Tel.: +55-(85)-3366-904

Abstract: Hydroxyapatite (HA) is a bioceramic very similar to the mineral component of bones and teeth. It is well established that osteoblasts grow better onto HA-coated metals than on metals alone. Herein, the preparation of a new system consisting of magnetite (Fe_3O_4) and HA functionalized with oleic acid and simvastatin (SIMV), and incorporated in chitosan (CHI) scaffolds, was undertaken. HA was synthesized by the hydrothermal method, while Fe_3O_4 was synthesized by co-precipitation. The polymer matrix was obtained using a 2% CHI solution, and allowed to stir for 2 h. The final material was freeze-dried to produce scaffolds. The magnetic properties remained unchanged after the formation of the composite, as well as after the preparation of the scaffolds, maintaining the superparamagnetism. CHI scaffolds were analyzed by scanning electronic spectroscopy (SEM) and showed a high porosity, with very evident cavities, which provides the functionality of bone growth support during the remineralization process in possible regions affected by bone tissue losses. The synthesized composite showed an average particle size between 15 and 23 nm for particles (HA and Fe_3O_4). The scaffolds showed considerable porosity, which is important for the performance of various functions of the tissue structure. Moreover, the addition of simvastatin in the system can promote bone formation.

Keywords: hydroxyapatite; magnetite; scaffolds; nanocomposite; simvastatin

Citation: Chaves, A.V.; Freire, R.M.; Feitosa, V.P.; Ricardo, N.M.P.S.; Denardin, J.C.; Andrade Neto, D.M.; Fechine, P.B.A. Hydroxyapatite-Based Magnetic Bionanocomposite as Pharmaceuticals Carriers in Chitosan Scaffolds. *J. Compos. Sci.* **2021**, *5*, 37. https://doi.org/10.3390/jcs5020037

Academic Editor: Francesco Tornabene

Received: 23 December 2020
Accepted: 18 January 2021
Published: 21 January 2021

Publisher's Note: MDPI stays neutral with regard to jurisdictional claims in published maps and institutional affiliations.

Copyright: © 2021 by the authors. Licensee MDPI, Basel, Switzerland. This article is an open access article distributed under the terms and conditions of the Creative Commons Attribution (CC BY) license (http://creativecommons.org/licenses/by/4.0/).

1. Introduction

Natural and synthetic bioceramics calcium phosphates are currently presented as one of the main materials used in medicine and dentistry. They are applied to the repair of bone loss due to their physical, chemical, and biological characteristics, which stimulates an adequate response of living tissue [1].

The wide acceptance of the bioceramics based on calcium phosphate occurs mainly due to its high degree of biocompatibility, which is related to its chemical similarity to the compounds normally found in the bone tissue [2]. Bioceramics with an improved performance presented in the literature are bioactive glasses, alumina (Al_2O_3), beta-tricalcium phosphate (β-TCP) and hydroxyapatite ($Ca_{10}(PO_4)_6(OH)_2$), HA) [3]. Among these, the last one (HA) is the most studied, the principal inorganic constituent of bone matrix and teeth,

which achieves optimal biocompatibility and is suitable for osteoblasts growing [4,5]. Due to the superficial roughness, HA may further increase the adhesion of osteoblasts, its proliferation and differentiation, thereby providing faster bone regeneration [6–8].

Recently, the use of magnetic nanoparticles (MNPs) for biological and medical purposes has been extensively explored, and their biocompatibility is overall validated by studies depending on their composition [9–11]. MNPs are applicable in various types of reaction e.g., magnetic hyperthermia, magnetic resonance contrast, the delivery of magnetic drugs and mechanical sensory cells receptors manipulated to induce cell differentiation, among others [12–14]. The limitations on the use of external magnetic fields can be overcome by introducing internal magnets located in the vicinity of the target by minimally invasive surgery or by using a superparamagnetic scaffold under the influence of an externally applied magnetic field [15,16]. In this sense, the magnetite (Fe_3O_4) phase can be described as a good example of MNPs. It has low toxicity, biocompatibility, superparamagnetism, reduces agglomeration in the biological medium, and assures clinically safe applications [17]. Due to these properties, MNPs have been used effectively in bone tissue repair treatment [18].

The polymeric scaffolds are usually biodegradable polymers or copolymers applied as biomaterials, sometimes produced from renewable sources such as corn, chitosan (CHI), cellulose, chitin and others [19]. Synthetic polymeric materials have been widely used in disposable medical supplies, prosthetic materials, dental materials, implants, and drug-delivery systems, while porous polymers have been widely used in the biomaterials field to produce membranes, supports for cell growth and implants [19]. Li and coworkers in recent studies have shown that the use of MNPs in polymers associated with bioceramics has been able to promote bone activity and growth [20].

The presence of simvastatin (SIMV) in calcium phosphates bioceramic composites was found to be very effective in bone regeneration [21]. Sun and coworkers conducted a study proving the action of SIMV associated with HA in providing new bone formation [22]. Therefore, the potential use of such a combination in medicine could be applied for instance, in the repair of bone defects caused by intra-osseous lesions, fractures, or as adjuncts in periodontal therapy as well as assisting the osteointegration process [23]. Therefore, this paper aimed to develop a novel biocomposite as a therapeutic agent that can provide a more efficient and direct treatment for bone defects. Each component was carefully chosen to obtain the best response, regarding the regeneration process. Such nanoparticles (NPs) are based on Fe_3O_4 composite coated with HA, oleic acid, and simvastatin, embedded in a polymeric matrix of chitosan (CHI) as a potential biomaterial to be applied in bone repair treatment. This work was written according to the International System of Units (SI).

2. Materials and Methods

2.1. Materials

Acetic acid (99.7%), ammonium hydroxide (29%), calcium chloride (II) dihydrate **(**$CaCl_2{\cdot}2H_2O$), iron chloride (III) hexahydrate ($FeCl_3{\cdot}6H_2O$), oleic acid (OA), iron sulfate heptahydrate ($FeSO_4{\cdot}7H_2O$) and phosphoric acid (H_3PO_4, 85%) were purchased from Dinâmica Química. Ammonium chloride (NH_4Cl), hydrochloric acid (HCl, 37%), acetonitrile (ACN, 99.8%) and chloroform (99.8%) were purchased from Vetec Química. All of them were used without further purification.

2.2. Synthesis of Fe_3O_4 Nanoparticles

The synthesis of MNPs was carried out following the methodology used by Barreto et al. [24]. Briefly, 30 mL of Milli-Q®® water was acidified in a beaker with 5% HCl solution until pH adjustment between 3 and 4 under constant stirring at 70 °C. Thereafter, metal salts were weighed and dissolved in Milli-Q®® water as precursors of Fe^{+2} and Fe^{+3} in a

molar ratio of 1:2, respectively. For this, 1.08 M $FeCl_3 \cdot 6H_2O$ and 0.54 M $FeSO_4 \cdot 7H_2O$ aqueous solutions were produced and heated in a previously acidified solution. A 5% NH_4OH solution was added to adjust the pH to 10. After the adjustment, a black precipitate was observed, which denotes the formation of magnetite. The reaction that occurred during this process can be summarized as follows:

$$Fe^{2+}_{(aq)} + 2Fe^{3+}_{(aq)} + 8OH^{-}_{(aq)} \rightarrow Fe_3O_{4(s)} + 4H_2O_{(l)} \quad (1)$$

After 30 min of stirring, the mixture containing the black precipitate was naturally cooled to room temperature. Magnetic decantation was used to separate the product, and then the solution was discarded. The process was repeated several times to wash the material using Milli-Q®® water and methanol. Finally, the powder was dried and stored under a vacuum for further application and characterization.

2.3. HA Synthesis via Hydrothermal Treatment

The required concentration of H_3PO_4 and $CaCl_2 \cdot 2H_2O$ solution was mixed under stirring to obtain a Ca/P molar ratio equals 1.67. After this, a white precipitate was formed by adding NH_4OH solution to adjust the pH to 9. The white suspension was stirred for 2 h. The precipitate was washed with Milli-Q®® water and vacuum filtered. The powder was then re-suspended in a solution of NH_4Cl 0.1 M, with the pH maintained at 9 to undergo the hydrothermal bath. The weight ratio between the precipitate and the solution in this step was 1:10. The suspension was transferred for a Teflon autoclave with a stainless steel support to receive the hydrothermal treatment at 150 °C for 5 h. After this, the autoclave was cooled to room temperature and the product was filtered, washed, and dried at 80 °C [25]. Equation (2) describes the synthesis of HA.

$$10CaCl_{2(aq)} + 6H_3PO_{4(aq)} + 2NH_4OH_{(aq)} \rightarrow Ca_{10}(PO_4)_6(OH)_{2(s)} + 18HCl_{(aq)} + 2NH_4Cl_{(aq)} \quad (2)$$

2.4. Composite Synthesis Fe_3O_4—HA

The first step for the synthesis of magnetic composite consists primarily of the production of Fe_3O_4 through co-precipitation. Thus, the iron oxide was dispersed in the 0.5 M $CaCl_2 \cdot 2H_2O$ solution under constant agitation using a mechanical stirring. Afterward, 0.3 M H_3PO_4 were slowly dripped, maintaining a Ca/P molar ratio equals 1.67, and then 5% (*v*/*v*) NH_4OH was used to adjust the pH to 9.0. In this step, the color of the solution changed from black to gray. The precipitate was separated by filtration, washed, and dried. The dry powder was dispersed in 0.1 M NH_4Cl (90% *w*/*w*) and the solution was transferred to a Teflon-lined autoclave to perform the hydrothermal treatment (150 °C for 5h). Finally, the product was filtered, washed, and dried at 80 °C. The weight ratio of the composite was 90:10 (HA:Fe_3O_4) [26].

2.5. Surface Modification of Fe_3O_4—HA with Oleic acid (Fe_3O_4—HA@OA)

500 mg of the synthesized magnetic nanocomposite were dispersed in 50 mL of chloroform using an ultrasonic treatment for 30 min, is then heated until it reached 75 °C. Afterward, 4 mL of OA was slowly added, and the mixture was mechanically stirred for 30 more minutes. The mixture was centrifuged at 3000× *g* rpm for 20 min and the precipitate was washed repeatedly with distilled water and ethanol. Finally, the product was dried at room temperature and stored under vacuum.

2.6. Simvastatin Adsorption on the Surface of Fe_3O_4—HA@OA

First, some commercially available pharmaceutical capsules (Sinvasmax®, Globo Laboratory, São José da Lapa, Brazil) were macerated, and the powder was dispersed in 20 mL of acetonitrile (ACN). Unlike the excipient, SIMV is soluble in acetonitrile. Thus, the suspension was filtered to collect the excipient (insoluble solid), separating the SIMV, which was recrystallized at room temperature, macerated, and stored under vacuum and

darkness. After this, in a falcon tube, 100 mg of previously synthesized Fe_3O_4—HA@OA was mixed with 10 mL solution of 2000 μg.mL^{-1} SIMV/ACN. The tube was subjected to strong horizontal stirring with shaker equipment for 24 h. Figure 1 describes the process of synthesis and adsorption of the drug in the composite.

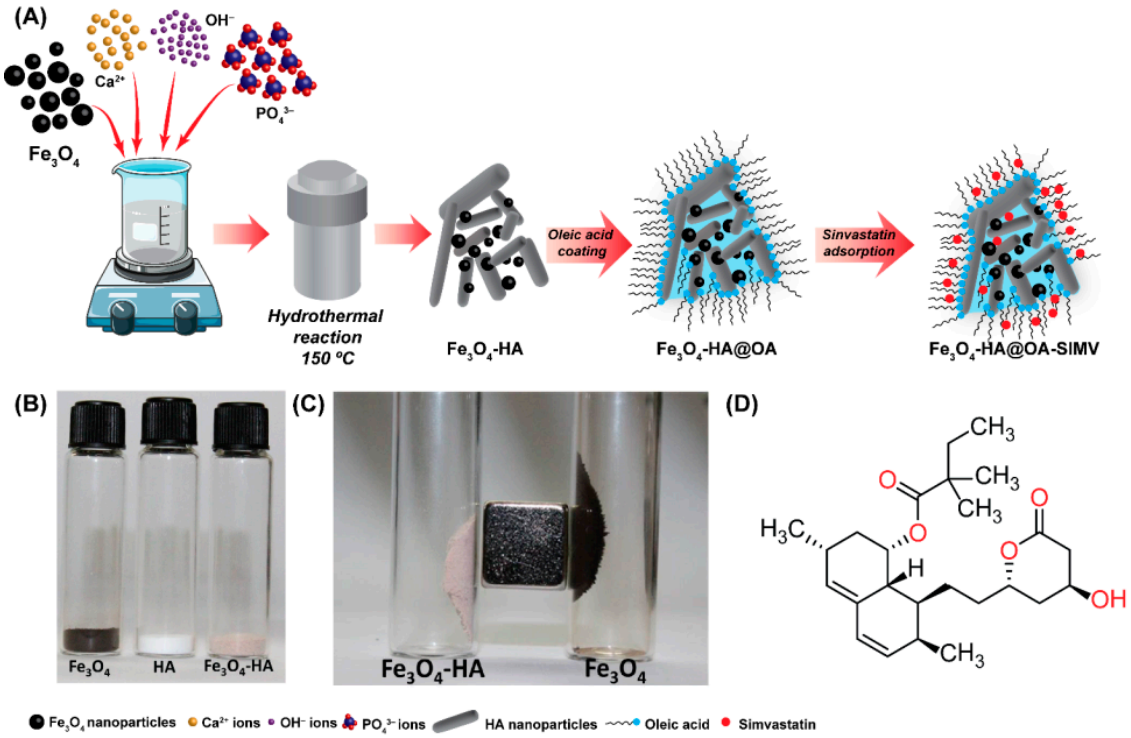

Figure 1. (**A**) Schemes for the synthesis of the nanomaterials prepared in this work. Macroscopic aspect of the samples Fe_3O_4, HA, and Fe_3O_4-HA (**B**) without and (**C**) under magnetic field. (**D**) Chemical structure of the Simvastatin.

2.7. Preparation of Chitosan Scaffolds with Fe_3O_4—HA@OA-SIMV

4 g of chitosan (Sigma-Aldrich, deacetylation degree 86%), low molecular weight powder, was dissolved in 200 mL of acetic acid solution 1% (*v*/*v*) under vigorous stirring for 3 h. Then, the solution was centrifuged at 4000 rpm for 30 min for the separation of possible impurities [27]. Using this solution as a solvent, 0.8 g of the composite was dispersed in 8 g of CHI solution. The mixture was sonicated for 30 min and then transferred to the template (5 cm × 5 cm). Finally, the filled template was frozen and lyophilized to obtain the scaffold.

2.8. Characterizations

The structural analysis and verification of the single-phase nature of the samples were obtained using X-ray diffraction (XRD). These measurements were carried out using XPert Pro MPD—Panalytical X-ray diffractometer equipped with CuKα radiation tube (k = 1.5406 Å) operated at a voltage of 30 kV and current of 15 mA. The identification analysis phase was conducted by comparing powder diffractograms with standard patterns from the International Centre for Diffraction Data (ICDD). The Rietveld refinement procedure [28] was applied to all diffraction patterns using the DBWS 2.4 [29]. The average crystallite sizes of NPs were calculated from the XRD data using the Scherrer equation.

The samples were also surveyed through Fourier-transform infrared (FTIR) spectra. The samples were macerated and pressed with KBr to form tablets with a 1:10 (sample:KBr) ratio. The spectra were obtained between 4000 and 400 cm^{-1} in a FTIR spectrophotometer (FTIR 8300, Shimadzu, Tokyo, Japan) by using 2 cm^{-1} resolution and 32 scans per analyzes.

The magnetic measurements were obtained using a vibrating sample magnetometer (Cryogenic VSM 5 Tesla system, Machida-shi, Tokyo, Japan) with a magnetic field of 5 Tesla and the temperature range 2–300 K (Department of Physics, University of Santiago de Chile—USACH). The VSM had been previously calibrated using a pure Ni wire, and, after measuring the mass of each sample, the magnetization was given in emu·g^{-1}.

Transmission electron microscope (TEM) images were obtained using a JEOL JEM 2100 LaB6 (JEOL, Tokyo, Japan) operating at accelerating voltage equals 200 kV and equipped with a TV (Gatan ES500W); CCD (TVips-16 MP). TEM samples were prepared by drop-casting a hexane dispersion of the nanocrystals onto carbon and carbon-coated copper grids. After deposition, the samples were dried to a temperature of 60 °C overnight before the obtention of the images. These analyzes were carried out in partnership with the Università del Salento, Italy.

The characterization of the SIMV was done using the spectra in the ultraviolet region in the wavelength range 190–300 nm, using a solution of 16 mg/mL SIMV in ACN. The maximum absorption was compared with those reported in the literature.

The morphology and porosity of the functionalized nanocomposite were evaluated using microscopy scanning Quanta 450 FEG (FEI, Amsterdam, The Netherlands). The samples (scaffolds) were fixed on carbon tapes, and then air-dried and coated with a thin layer of gold to gain better conductivity, as is required for high-quality SEM imaging. The powder was fixed on silver glue and examined using the same instrument.

The thermogravimetric analysis (TGA) curves are usually obtained on TGA Q50 V20.13 Build 39 of thermal analysis (TA) Instruments at a heating rate of 10 °C min^{-1}, starting at room temperature to 950 °C in a dynamic atmosphere of nitrogen and flow 25 mL. min^{-1} alumina crucible and sample mass approximately 5.0 mg. The differential scanning calorimetry (DSC) curves were obtained on DSC Q20 V24.9 Build 121 equipment under a dynamic nitrogen atmosphere with a flow rate of 50 mL·min^{-1}, heating rate of 10 °C·min^{-1}, with heating from room temperature to 400 °C, partially closed aluminum pan and sample mass about 0.5 mg. The equipment must be calibrated with indium (MP 156.6 °C; $\Delta H_{melting}$ = 28.54 J·g^{-1}) and lead (MP 327.0 °C), or other standards recommended by the manufacturer. The purity by the DSC evaluation is performed by applying the Van't Hoff equation to the melting peak of the drug.

3. Results and Discussion

3.1. Structural Characterization.

3.1.1. XRD and FTIR Analysis

Figure 2a shows the XRD patterns of the synthesized NPs. The crystalline phases were examined by comparing the patterns with the ICDD database concerning the standard HA (ICDD/PDF: 01-072-1243). The HA shows higher crystallinity due to hydrothermal procedure and a single-phase, $Ca_{10}(PO_4)_6(OH)_2$ with a hexagonal crystal structure. The synthesis of Fe_3O_4 sample was successfully accomplished by comparing the results with the standard (ICDD/PDF: 00-001-1111) during the refinement (Figure 2a). The obtained crystallographic peaks, such as 30.09°; 35.44°; 43.07° and 62.55°, are relative to cubic space group Fd-3m crystal system representing the characteristics of a spinel structure (ICDD/PDF: 00-001-1111). The composite (Fe_3O_4-HA) presents peaks predominantly of HA in 25.87° and 31.74°, again well-defined due to hydrothermal treatment, as well as some peaks observed with Fe_3O_4 that appeared smaller and were recording accurately at the peak in 35.44°.

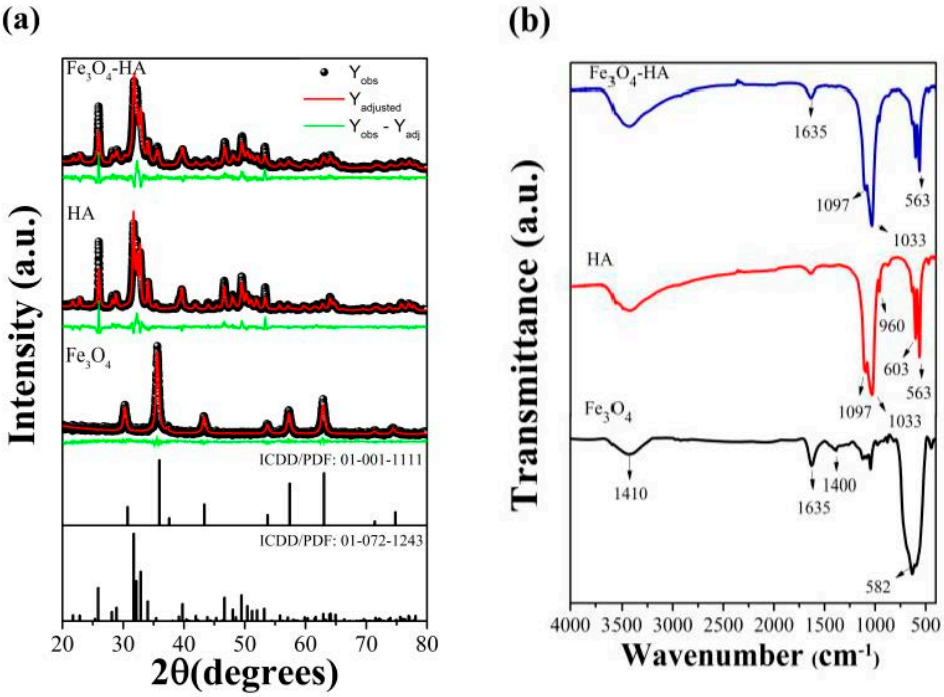

Figure 2. (**a**) X-ray diffraction (XRD) pattern of the Fe_3O_4, HA, and Fe_3O_4-HA; (**b**) Fourier-transform infrared (FTIR) spectra of the respective samples.

Additionally, one might note that in the Rietveld method, some of the most important data to be evaluated are the R_{WP} (by obtaining the error percentage) and S (ratio of error provided by the expected error), since they refer to the agreement and the progress of refinement (Table 1) [30,31]. The observed peaks are approximately coincident with the calculated peaks, which can be seen in a line representing the difference between the intensity observed and intensity calculated (Figure 2a). This justifies the values shown in Table 1 and demonstrates the satisfactory character of refinement.

Table 1. X-ray diffraction (XRD**)** patterns structural results through Rietveld refinement of HA, Fe_3O_4, and Fe_3O_4-HA samples.

Sample	Crystalline Phase	Mass (%)	Lattice Parameters			R_{wp} (%)	S	V(Å³)	Density (g·cm⁻³)	Width (nm)
			a (Å)	b (Å)	c (Å)					
HA	$Ca_{10}(PO_4)_6(OH)_2$	100	9.4713	9.4713	6.8669	13.81	1.89	533.484	3.122	18.37 (±0.39)
Fe_3O_4	Fe_3O_4	100	8.3615	8.3615	8.3615	14.91	0.91	548.598	5.263	15.5 (±0.32)
Fe_3O_4-HA	$Ca_{10}(PO_4)_6(OH)_2$	93.7	9.4439	9.4439	6.8769	11.16	1.48	531.175	3.135	18.37 (±0.34)
	Fe_3O_4	6.3	8.3562	8.3562	8.3562			583.496	5.273	22.53 (±0.74)

According to the calculated data presented in Table 1, it was shown that the average crystallite sizes of the samples were 18.37 nm for HA, 15.5 nm for Fe_3O_4 and 22.53 nm for the composite. It was observed that the particle dimensions presented small variation even after the formation of the composite, maintaining its size on a nanometric scale. A similar size in the refinement by the Rietveld method has been reported in the literature [32].

Figure 2b shows the FTIR spectra of precursors (Fe_3O_4 and HA) to confirm the binding band assignments of the synthesized compounds. Regarding the Fe_3O_4, bands related

to the bonds for iron spinel were observed, with a wavenumber of 582 cm^{-1}, referring to the stretching of the Fe bonds in the tetrahedral site, 1400 cm^{-1} referring to the angular vibration related to the Fe-O bond, 1635 cm^{-1} and 3410 cm^{-1} agreeing with the angular vibration and stretching of OH bonds respectively [33,34]. All vibrational modes of the HA functional groups were identified. The very strong bands observed in 1097 and 1033 cm^{-1}, respectively, were associated with vibrational stretches outside the P-O plane, whereas the weak band centered in 960 cm^{-1} was attributed to the symmetrical stretch vibration of O-P-O. Strong O-P-O vibrational waves can be seen in the wavenumbers between 563 and 603 cm^{-1} [35,36]. In this way, the characteristic bands of the two materials are also identified in the Fe_3O_4-HA spectra.

3.1.2. Magnetization Measurements

The magnetization curves were used to investigate the magnetic properties of the nanocomposite. In this sense, Figure 3a,b displayed the measurements recorded at room temperature for Fe_3O_4 and Fe_3O_4-HA, respectively. The absence of hysteresis was observed for both nanomaterials, which indicates a superparamagnetic behavior [37,38]. However, the Fe_3O_4-HA nanocomposite was found to have inferior magnetic properties compared to Fe_3O_4 NPs. This can be explained by the presence of non-magnetic material [39]. Therefore, the HA component does not affect the magnetic nature of the composite. However, its influence on the saturation magnetization (M_s) is clear, since the non-magnetic mass was taking into consideration to normalize the M parameter. Due to this, Fe_3O_4 and Fe_3O_4-HA present M_s values of 39.78 and 4.85 $emu \cdot g^{-1}$.

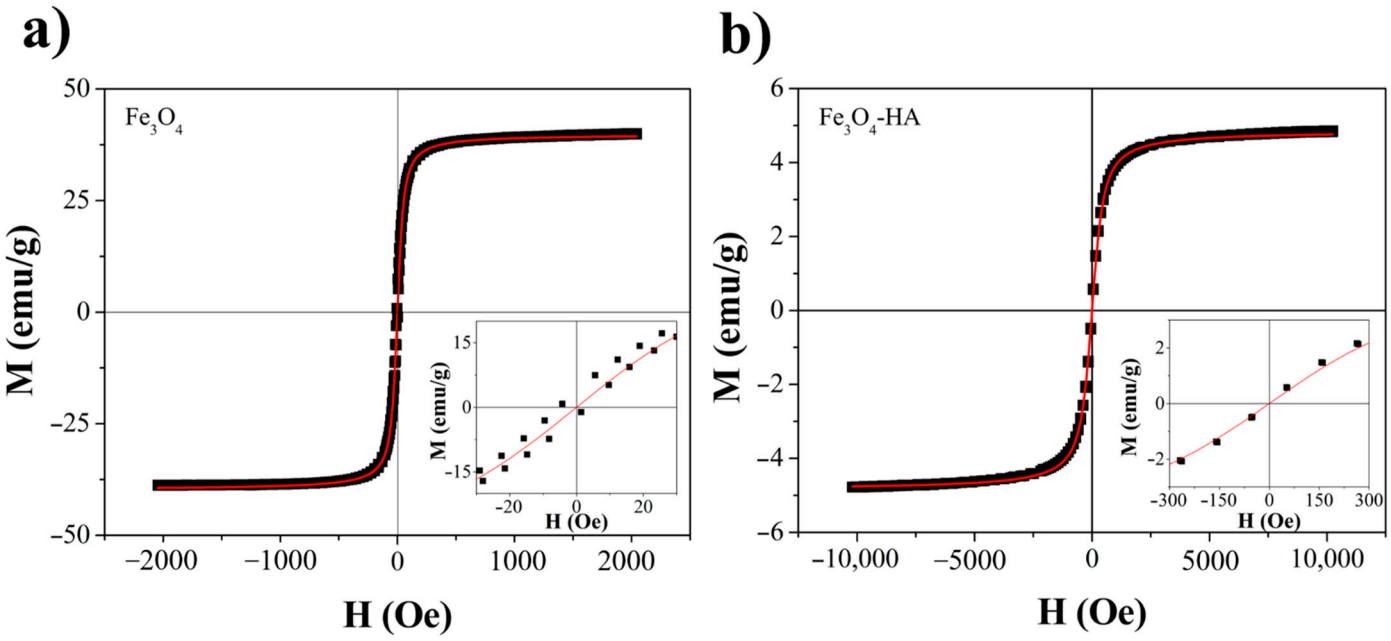

Figure 3. Magnetization measurements of (**a**) the Fe_3O_4 and (**b**) Fe_3O_4-HA samples. The red line denotes the description of the experimental data using the Langevin function.

To deepen further our study, the experimental data obtained through magnetic measurements of the samples were described by the Langevin function [40], using the following equation:

$$M = N\mu^2 H/3K_B T \quad (3)$$

where N, K_B, T e H indicates, respectively, the number of the ions of Fe^{2+}, Boltzmann constant, temperature, and the magnetic field applied. By using this function, an average diameter related to the magnetic-ordered structure (d_L) can also be inferred by setting a parameter $a = m/K_B$. Once this parameter was calculated, the d_L was obtained using $a =$

$4p(d_L/2)^3 M_0/3K_B$ [41]. It was observed that the particle sizes found by the magnetization curve crystallites are close to the values found by the PXRD, showing an approximate average size of 13.3 nm to Fe_3O_4 and 27.5 nm to Fe_3O_4-HA.

3.1.3. TEM

Figure (4A–C) shows TEM images for Fe_3O_4, HA, and Fe_3O_4-HA. The sample Fe_3O_4 is composed by NPs with pseudo spherical morphology, which is expected for Fe_3O_4 NPs synthesized by co-precipitation using NH_4OH (Figure 4A) [42,43]; while HA NPs exhibited rod-like morphology (Figure 4B), which corroborates with a *c*-axis preferential orientation demonstrated by the XRD; and for the sample Fe_3O_4-HA we could evidence NPs with morphologies such as Fe_3O_4 and HA, as pointed with green and red arrows (Figure 4C). TEM analysis confirms that the mixture of the two components of the magnetic composite is mixed without the core-shell structure. However, even without the core-shell structure, we demonstrated that the magnetic composite behaved, as a whole, as magnetic material, as shown in Figure 1 C in Section 2.6.

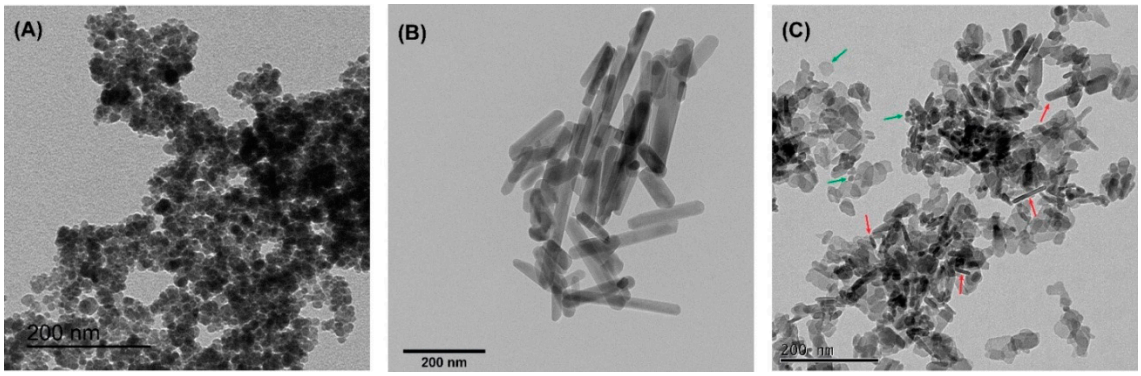

Figure 4. Transmission electron microscopy (TEM) micrographs of the samples (**A**) Fe_3O_4, (**B**) HA and (**C**) Fe_3O_4-HA. All bars correspond to 200 nm.

XRD refinement indicated that the biomaterial is composed of 93.5% of hydroxyapatite and 6.5% of Fe_3O_4 (Table 1). However, in Figure 4, it is possible to see that the number of NPs with rod-like morphology does not correspond to the molar fraction found in the XRD. This indicates that the presence of Fe_3O_4 in the reaction medium to produce HA affected the growth of HA NPs, decreasing the *c*-axis preferential orientation. This fact was also demonstrated in XRD refinement. Therefore, our results suggest that physical interaction occurred between Fe_3O_4 and HA, probably through electrostatic interactions.

3.1.4. Thermal Analysis

Simvastatin was characterized using the DSC technique for measuring the heat flow difference between a substance and a reference material as a function of a heating or cooling program. This thermal characterization and determination of the purity of drugs are widely used in the pharmaceutical industry [44]. The DSC curve of the SIMV (Figure 5a) shows the first endothermic event at temperatures ranging from 52.46 °C with power consumption, which probably refers to the boiling point of the solvent used in the recrystallization, in this case, ACN. The second event, characteristic of the melting process of the substance, SIMV, starts at 122.85 °C, with power consumption. Thus, according to the curve, SIMV showed a melting temperature of 134.5 °C. The spectrum in the ultraviolet (UV) region is shown in Figure 5b and agrees with the spectrum described in the literature for simvastatin absorption maxima at 231, 238, and 247 nm [45].

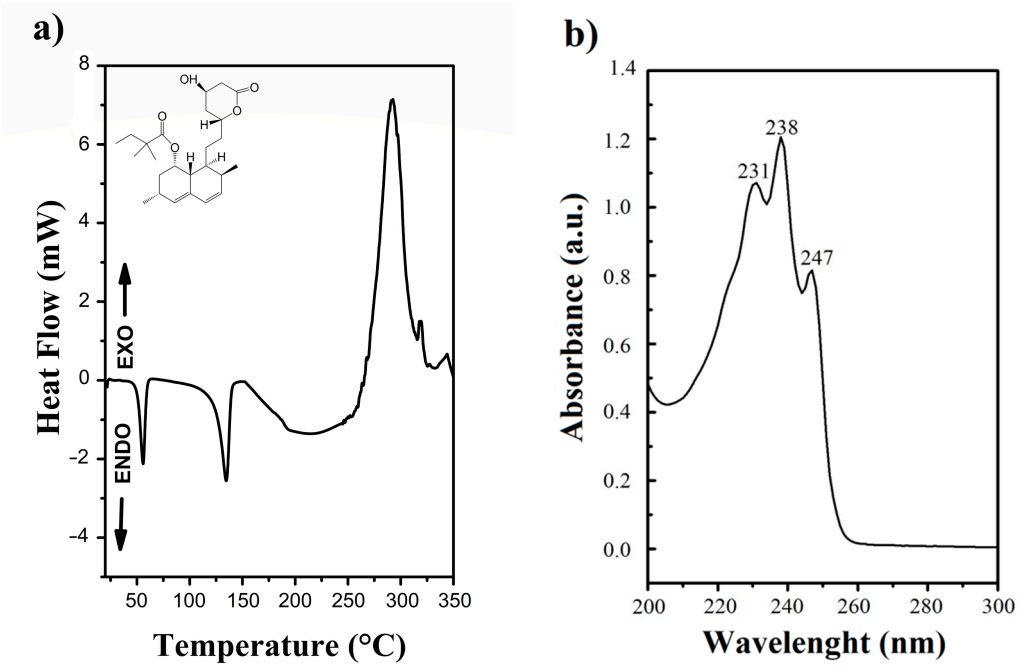

Figure 5. (**a**) Differential scanning calorimetry (DSC) and (**b**) Absorption spectra in the ultraviolet region of simvastatin (SIMV).

The melting point of SIMV, according to the literature, ranging from 135–138 °C [46]. Therefore, the purity of this drug recrystallized showed up around 94.37 to 97.53%.

The TGA of the modified sample was performed to verify the presence of oleate and SIMV molecules through mass-loss events. Therefore, Figure 6 shows the thermograms of samples with and without surface modification, respectively. The first thermogram indicates that up to 850 °C, the weight loss of Fe_3O_4-HA is 5.8% of the original. Furthermore, the thermogram finds the stability at elevated temperatures of bioceramic [47]. Initially, the loss corresponds to the thermal desorption of water from the surface of NP. Near 200 °C, the weight loss is attributed to the elimination of structural H_2O lattice. This long-range of temperature, which occurs in weight loss, indicates that the water does not interact evenly with the structure, which is compatible with the existence of different structural sites. The total mass loss for the sample modified with OA was 10.75%. The slight weight loss observed next to 250 °C indicates some OA molecules were adsorbed on the sample surface Fe_3O_4-HA@OA (Figure 6b) [48].

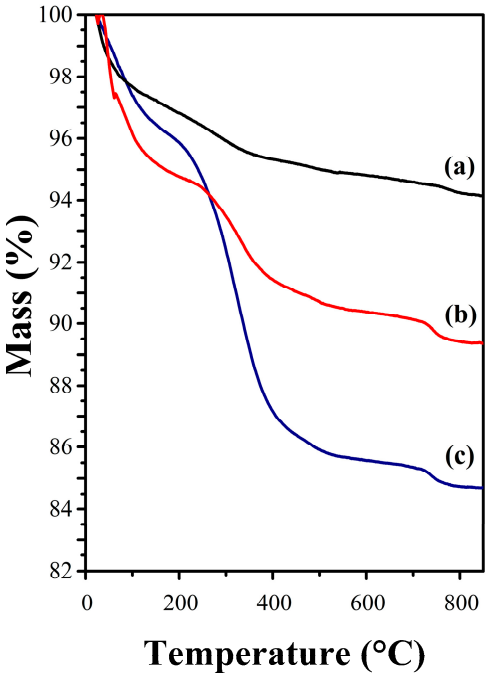

Figure 6. Thermogravimetric analysis of (**a**) Fe_3O_4-HA, (**b**) Fe_3O_4-HA@OA, and (**c**) Fe_3O_4-HA@OA-SIMV.

However, any weight loss above 400 °C may indicate distinct oleate interactions between molecules and atoms' surface, leading to differences in the intensities of these interactions. Therefore, it is possible to determine that the weight loss compared to OA was 5.85%, i.e., the amount of the OA adsorbed on Fe_3O_4-HA@OA sample is approximately this value. The thermogram shows four events for functionalized composite samples with SIMV, indicating the presence of physiosorbed species, total weight loss of 15.4%. In the temperature range of approximately 175–600 °C, in which 14.5% of the mass was eliminated, three events can be attributed to SIMV decomposition and loss of OA chemisorbed and physiosorbed. Figure 6 also shows a comparison between the thermograms of the three samples, presenting the different weight losses. The improved thermal stability given by the Fe_3O_4-HA indicates that the incorporation of OA and SIMV on their surface was successfully carried out and it possibly indicates that the weight loss of SIMV was 4.65% compared to composites with and without this drug.

3.2. Chitosan Bionanocomposite.

SEM micrographs of the pure CHI matrix and CHI/Fe_3O_4-HA@OA-SIMV bionanocomposite are presented in Figure 7a,c), respectively. The micron-size elements are distributed in the scaffold. The visualization of nano-sized particles is not possible in Figure 7, but can be observed on grains with the presence of all chemical items for the magnetic composite structures and the CHI matrix in the micrographs.

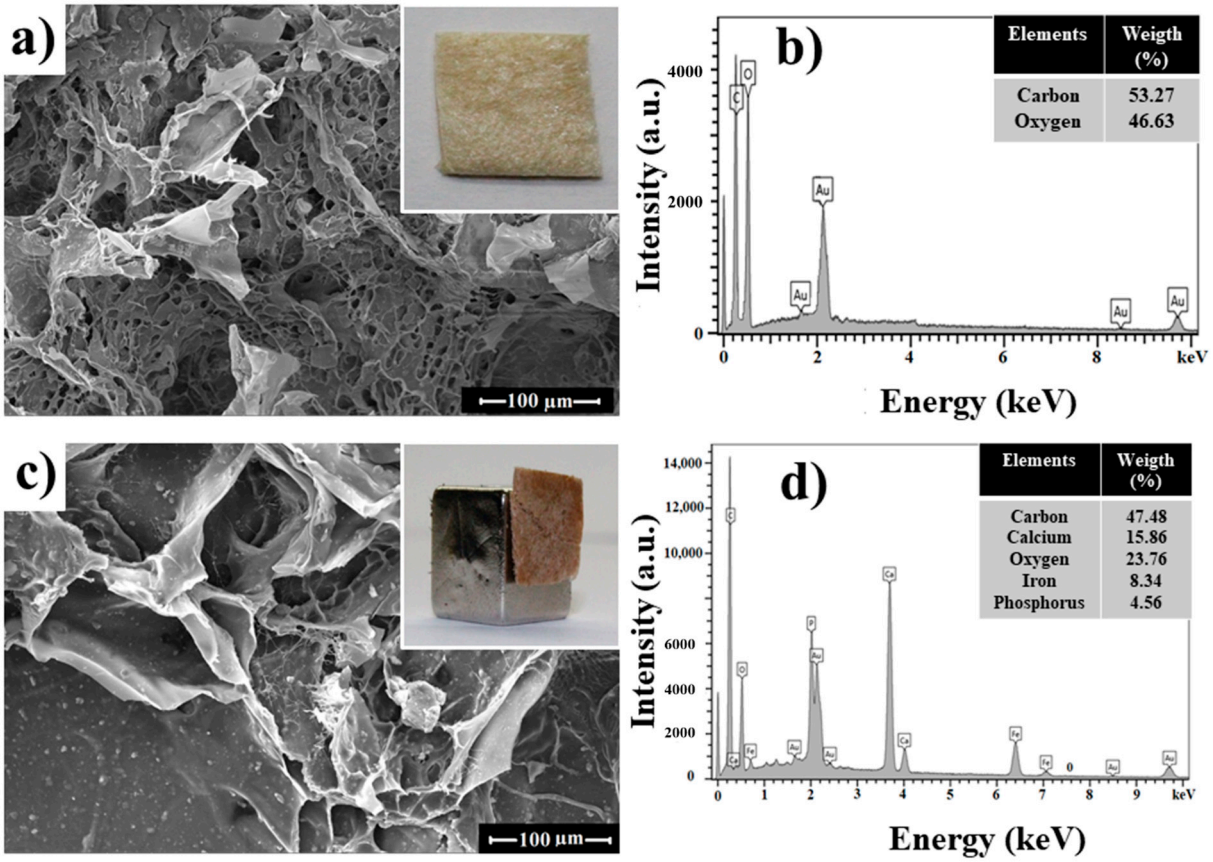

Figure 7. Scanning electron microscope images of (**a**) Pure CHI matrix, (**b**) Energy-dispersive X-ray (EDX) spectroscopy of pure CHI matrix, (**c**) CHI/Fe_3O_4—HA@AO-SIMV, and (**d**) EDX spectra of CHI/bionanocomposite with the respective elements and weight percentage.

It is possible to verify the high porosity of the scaffold distributed all over the area of the polymer, which benefits a better efficiency of the composite face to magnetic material adhesion, and the degradability and assimilation function in the bone area to be regenerated. The chemical analysis by energy-dispersive X-ray (EDX) (Figure 7b,d) showed the chemical elements of the CHI matrix and the presence of iron, calcium, and phosphate ions in the bionanocomposite respectively, including through CHI fibers. This allows us to infer that the NPs were distributed all over the scaffold matrix.

4. Conclusions

The hydroxyapatite-based magnetic composite functionalized with OA and simvastatin was synthesized according to the proposed methodology, in addition to the production of CHI scaffolds and their incorporation of the composite. Based on VSM, as well as particle size analysis by diffraction, the size of magnetite with hydroxyapatite NPs was in the range of 15–30 nm. According to the TEM images, the size of the particles was 40–60 nm; and the SEM images showed the presence of all compounds synthesized, in addition to showing high porosity of the scaffolds. The magnetization of the composite after the addition of HA suggests that the structure of magnetite remained unchanged at around 4.85 emu·g^{-1}. The adsorption of SIMV on the composite can be observed in the TGA, which showed a total weight loss of 4.65% of this drug. The literature review supports the hypothesis that the compounds used in this work induce osteogenesis and the production of a magnetic composite, aiming at the creation of better material, capable of being applied in bone regeneration in the future. Therefore, the association of SIMV with calcium phosphates and magnetite encourages research in the area of tissue engineering.

Author Contributions: Conceptualization, A.V.C., D.M.A.N. and P.B.A.F.; methodology, A.V.C., R.M.F., V.P.F., D.M.A.N. and P.B.A.F.; software, A.V.C., D.M.A.N. and P.B.A.F.; validation, A.V.C., and P.B.A.F.; formal analysis, A.V.C., D.M.A.N., R.M.F. and P.B.A.F.; investigation, A.V.C., N.M.P.S.R., V.P.F., R.M.F. and P.B.A.F.; resources, A.V.C., J.C.D., N.M.P.S.R. and P.B.A.F.; data curation, A.V.C. and P.B.A.F.; writing—original draft preparation, A.V.C.; writing—review and editing, A.V.C. and P.B.A.F.; visualization, R.M.F., D.M.A.N. and P.B.A.F.; supervision, V.P.F and P.B.A.F.; project administration, A.V.C. and P.B.A.F.; funding acquisition, P.B.A.F., V.P.F., N.M.P.S.R. and J.C.D. All authors have read and agreed to the published version of the manuscript.

Funding: This work was partly funded by the Brazilian and Chilean agencies for scientific and technological development: CAPES (Finance Code 001-PROEX 2038.000509/2020-82), CNPq (408790/2016-4), Funcap (PNE-0112-00048.01.00/16). Fondecyt (1200782 and 3170240) and Basal CEDENNA (AFB180001 and FB0807).

Acknowledgments: The authors would like to acknowledge Central Analítica-UFC/CT-INFRA/MCTI-SISANO/Pró-Equipamento and X-ray Diffraction Laboratory (UFC).

Conflicts of Interest: The authors declare no conflict of interest. The funders had no role in the design of the study; in the collection, analyses or interpretation of data; in the writing of the manuscript or in the decision to publish the results.

References

1. Zhou, Y.; Wu, C.; Chang, J. Bioceramics to regulate stem cells and their microenvironment for tissue regeneration. *Mater. Today* **2019**, *24*, 41–56, doi:10.1016/j.mattod.2018.07.016.
2. Meng, D.; Dong, L.; Yuan, Y.; Jiang, Q. In vitro and in vivo analysis of the biocompatibility of two novel and injectable calcium phosphate cements. *Regen. Biomater.* **2018**, *6*, 13–19.
3. Zhao, C.; Wu, C.; Chang, J. Advances in synthesis of calcium phosphate crystals with controlled size and shape. *Acta Biomater.* **2014**, *10*, 4071–4102, doi:10.1016/j.actbio.2014.06.017.
4. Moura, N.K.D.; Siqueira, I.A.; Machado, J.P.D.B.; Kido, H.W.; Avanzi, I.R.; Rennó; ACM; Trichês, E.D.S.; Passador, F.R. Production and Characterization of Porous Polymeric Membranes of PLA/PCL Blends with the Addition of Hydroxyapatite. *J. Compos. Sci.* **2019**, *3*, 45.
5. Pietrzykowska, E.; Romelczyk, B.; Wojnarowicz, J.; Sokolova, M.; Szlązak, K.; Święszkowski, W.; Locs, J.; Lojkowski, W. Preparation of a Ceramic Matrix Composite Made of Hydroxyapatite Nanoparticles and Polylactic Acid by Consolidation of Composite Granules. *Nanomaterials* **2020**, *10*, 1060, doi:10.3390/nano10061060.
6. Martinelli, N.M.; Ribeiro, M.J.G.; Ricci, R.; Marques, M.A.; Lobo, A.O.; Marciano, F. In Vitro Osteogenesis Stimulation via Nano-Hydroxyapatite/Carbon Nanotube Thin Films on Biomedical Stainless Steel. *Materials* **2018**, *11*, 1555.
7. Zakrzewski, W.; Dobrzyński, M.; Rybak, Z.; Szymonowicz, M.K.; Wiglusz, R.J. Selected Nanomaterials' Application Enhanced with the Use of Stem Cells in Acceleration of Alveolar Bone Regeneration during Augmentation Process. *Nanomaterials* **2020**, *10*, 1216, doi:10.3390/nano10061216.
8. Jiang, P.; Zhang, Y.; Hu, R.; Wang, X.; Lai, Y.; Rui, G.; Lin, C. Hydroxyapatite-modified micro/nanostructured titania surfaces with different crystalline phases for osteoblast regulation. *Bioact. Mater.* **2021**, *6*, 1118–1129, doi:10.1016/j.bioactmat.2020.10.006.
9. Moise, S.; Céspedes, E.; Soukup, D.; Byrne, J.; El Haj, A.J.; Telling, N.D. The cellular magnetic response and biocompatibility of biogenic zinc- and cobalt-doped magnetite nanoparticles. *Sci. Rep.* **2017**, *7*, 39922, doi:10.1038/srep39922.
10. Samrot, A.V.; Sahithya, C.S.; Selvarani A, J.; Purayil, S.K.; Ponnaiah, P. A review on synthesis, characterization and potential biological applications of superparamagnetic iron oxide nanoparticles. *Curr. Res. Green Sustain. Chem.* **2021**, *4*, 100042, doi:10.1016/j.crgsc.2020.100042.
11. Tufani, A.; Qureshi, A.; Niazi, J.H. Iron oxide nanoparticles based magnetic luminescent quantum dots (MQDs) synthesis and biomedical/biological applications: a review. *Mater. Sci. Eng. C* **2020**, *118*, 111545, doi:10.1016/j.msec.2020.111545.
12. Gawali, S.L.; Shelar, S.B.; Gupta, J.; Barick, K.; Hassan, P. Immobilization of protein on Fe3O4 nanoparticles for magnetic hyperthermia application. *Int. J. Biol. Macromol.* **2021**, *166*, 851–860, doi:10.1016/j.ijbiomac.2020.10.241.
13. Mohammadi, M.; Aghaei, F.P. Magnetite Fe3O4 surface as an effective drug delivery system for cancer treatment drugs: density functional theory study. *J. Biomol. Struct. Dyn.* **2020**, doi:10.1080/07391102.2020.1754915.
14. Xia, Y.; Chen, H.; Zhao, Y.; Zhang, F.; Li, X.; Wang, L.; Weir, M.D.; Ma, J.; Reynolds, M.A.; Gu, N.; et al. Novel magnetic calcium phosphate-stem cell construct with magnetic field enhances osteogenic differentiation and bone tissue engineering. *Mater. Sci. Eng. C* **2019**, *98*, 30–41, doi:10.1016/j.msec.2018.12.120.
15. Vangijzegem, T.; Stanicki, D.; Laurent, S. Magnetic iron oxide nanoparticles for drug delivery: applications and characteristics. *Expert Opin. Drug Deliv.* **2019**, *16*, 69–78, doi:10.1080/17425247.2019.1554647.
16. Yan, Y.; Zhang, Y.; Zuo, Y.; Zou, Q.; Li, J.; Huang, J. Development of Fe3O4–HA/PU superparamagnetic composite porous scaffolds for bone repair application. *Mater. Lett.* **2018**, *212*, 303–306, doi:10.1016/j.matlet.2017.10.067.

17. Ribeiro, V.; Barreto, A.; DeNardin, J.C.; Mele, G.; Carbone, L.; Mazzetto, S.; Sousa, E.M.B.; Fechine, P.B. Magnetic nanoparticles coated with anacardic acid derived from cashew nut shell liquid. *J. Mater. Sci.* **2013**, *48*, 7875–7882, doi:10.1007/s10853-013-7477-4.
18. Fan, D.; Wang, Q.; Zhu, T.; Wang, H.; Liu, B.; Wang, Y.; Liu, Z.; Liu, X.; Fan, D.; Wang, X. Recent Advances of Magnetic Nanomaterials in Bone Tissue Repair. *Front. Chem.* **2020**, *8*, 745.
19. Jafari, M.; Paknejad, Z.; Rad, M.R.; Motamedian, S.R.; Eghbal, M.J.; Nadjmi, N.; Khojasteh, A. Polymeric scaffolds in tissue engineering: a literature review. *J. Biomed. Mater. Res. Part B Appl. Biomater.* **2017**, *105*, 431–459, doi:10.1002/jbm.b.33547.
20. Li, M.; Liu, J.; Cui, X.; Sun, G.; Hu, J.; Xu, S.; Yang, F.; Zhang, L.; Wang, X.; Tang, P. Osteogenesis effects of magnetic nanoparticles modified-porous scaffolds for the reconstruction of bone defect after bone tumor resection. *Regen. Biomater.* **2019**, *6*, 373–381, doi:10.1093/rb/rbz019.
21. Cruz, R.; Pesce, G.; Calasans-Maia, J.D.A.; Moraschini, V.; Calasans-Maia, M.D.; Granjeiro, J.M. Calcium Phosphate Carrying Simvastatin Enhances Bone Regeneration: A Systematic Review. *Braz. Dent. J.* **2020**, *31*, 93–102, doi:10.1590/0103-644020200297.
22. Sun, T.-W.; Yu, W.-L.; Qi, C.; Chen, F.; Zhu, Y.; He, Y. Multifunctional simvastatin-loaded porous hydroxyapatite microspheres/collagen composite scaffold for sustained drug release, angiogenesis and osteogenesis. *J. Control. Release* **2017**, *259*, e130, doi:10.1016/j.jconrel.2017.03.26.
23. Yu, W.-L.; Sun, T.-W.; Qi, C.; Zhao, H.-K.; Ding, Z.-Y.; Zhang, Z.-W.; Sun, B.-B.; Shen, J.; Chen, F.; Zhu, Y.; et al. Enhanced osteogenesis and angiogenesis by mesoporous hydroxyapatite microspheres-derived simvastatin sustained release system for superior bone regeneration. *Sci. Rep.* **2017**, *7*, 44129, doi:10.1038/srep44129.
24. Barreto, A.; Santiago, V.R.; Mazzetto, S.; DeNardin, J.C.; Lavín, R.; Mele, G.; Ribeiro, M.E.N.P.; Vieira, I.G.P.; Gonçalves, T.; Ricardo, N.M.P.S.; et al. Magnetic nanoparticles for a new drug delivery system to control quercetin releasing for cancer chemotherapy. *J. Nanoparticle Res.* **2011**, *13*, 6545–6553, doi:10.1007/s11051-011-0559-9.
25. Wang, L.; Weng, L.; Wang, L.; Song, S. Hydrothermal synthesis of hydroxyapatite nanoparticles with various counterions as templates. *J. Ceram. Soc. Jpn.* **2010**, 118, 1195–1198.
26. Panseri, S.; Cunha, C.; D'Alessandro, T.; Sandri, M.; Russo, A.; Giavaresi, G.; Marcacci, M.; Hung, C.T.; Tampieri, A. Magnetic Hydroxyapatite Bone Substitutes to Enhance Tissue Regeneration: Evaluation In Vitro Using Osteoblast-Like Cells and In Vivo in a Bone Defect. *PLoS ONE* **2012**, *7*, e38710, doi:10.1371/journal.pone.0038710.
27. Rodríguez-Vázquez, M.; Vega-Ruiz, B.; Ramos-Zúñiga, R.; Saldaña-Koppel, D.A.; Quiñones-Olvera, L.F. Chitosan and Its Potential Use as a Scaffold for Tissue Engineering in Regenerative Medicine. *BioMed Res. Int.* **2015**, *2015*, 1–15, doi:10.1155/2015/821279.
28. Rietveld, H.M. Line profiles of neutron powder-diffraction peaks for structure refinement. *Acta Crystallogr.* **1967**, *22*, 151–152, doi:10.1107/s0365110x67000234..
29. Bleicher, L.; Sasaki, J.M.; Santos, C.O.P. Development of a graphical interface for the Rietveld refinement program DBWS. *J. Appl. Crystallogr.* **2000**, *33*, 1189, doi:10.1107/s0021889800005410.
30. Cheng, G.; Zhang, Y.; Yin, H.; Ruan, Y.; Sun, Y.; Lin, K. Effects of strontium substitution on the structural distortion of hydroxyapatite by rietveld refinement and Raman Spectroscopy. *Ceram. Int.* **2019**, *45*, 11073–11078, doi:10.1016/j.ceramint.2019.02.194.
31. Pereira, G.F.L.; Costa, F.N.; Souza, J.A.; Haddad, P.S.; Ferreira, F.F. Parametric Rietveld refinement and magnetic characterization of superparamagnetic iron oxide nanoparticles. *J. Magn. Magn. Mater.* **2018**, *456*, 108–117, doi:10.1016/j.jmmm.2018.02.020.
32. Neto, D.A.; Carvalho, E.; Rodrigues, E.; Feitosa, V.P.; Sauro, S.; Mele, G.; Carbone, L.; Mazzetto, S.; Rodrigues, L.; Fechine, P.B. Novel hydroxyapatite nanorods improve anti-caries efficacy of enamel infiltrants. *Dent. Mater.* **2016**, *32*, 784–793, doi:10.1016/j.dental.2016.03.026.
33. Taufiq, A.; Nikmah, A.; Hidayat, A.; Sunaryono, S.; Mufti, N.; Hidayat, N.; Susanto, H. Synthesis of magnetite/silica nanocomposites from natural sand to create a drug delivery vehicle. *Heliyon* **2020**, *6*, e03784, doi:10.1016/j.heliyon.2020.e03784.
34. Freire, T.M.; Fechine, L.M.U.D.; Queiroz, D.; Freire, R.M.; DeNardin, J.C.; Ricardo, N.M.P.S.; Rodrigues, T.N.B.; Gondim, D.R.; Silva, I.J.; Fechine, P.B. Magnetic Porous Controlled Fe3O4–Chitosan Nanostructure: An Ecofriendly Adsorbent for Efficient Removal of Azo Dyes. *Nanomaterials* **2020**, *10*, 1194, doi:10.3390/nano10061194.
35. Miranda, M.; Torrecillas, R.; Fernández, A. Reactivity of Ca and P precursors to form hydroxyapatite and its influence on the properties of the obtained powders. *Ceram. Int.* **2020**, *46*, 27860–27865, doi:10.1016/j.ceramint.2020.07.284.
36. Daryan, S.H.; Khavandi, A.; Javadpour, J. Surface engineered hollow hydroxyapatite microspheres: Hydrothermal synthesis and growth mechanisms. *Solid State Sci.* **2020**, *106*, 106301, doi:10.1016/j.solidstatesciences.2020.106301.
37. Wierzbinski, K.R.; Szymanski, T.; Rozwadowska, N.; Rybka, J.D.; Zimna, A.; Zalewski, T.; Nowicka-Bauer, K.; Malcher, A.; Nowaczyk, M.; Krupinski, M.; et al. Potential use of superparamagnetic iron oxide nanoparticles for in vitro and in vivo bioimaging of human myoblasts. *Sci. Rep.* **2018**, *8*, 1–17, doi:10.1038/s41598-018-22018-0.
38. Neto, D.M.A.; Freire, R.M.; Gallo, J.; Freire, T.M.; Queiroz, D.C.; Ricardo, N.M.P.S.; Vasconcelos, I.F.; Mele, G.; Carbone, L.; Mazzetto, S.E.; et al. Rapid Sonochemical Approach Produces Functionalized Fe3O4 Nanoparticles with Excellent Magnetic, Colloidal, and Relaxivity Properties for MRI Application. *J. Phys. Chem. C* **2017**, *121*, 24206–24222, doi:10.1021/acs.jpcc.7b0494.
39. De Menezes, F.L.; Andrade Neto, D.M.; Rodrigues, M.D.L.L.; Lima, H.L.S.; Paiva, D.V.M.; da Silva, M.A.S.; Fechine, L.M.U.D.; Sombra, A.S.B.; Freire, R.M.; Denardin, J.C.; Rosa, M.D.F. From Magneto-Dielectric Biocomposite Films to Microstrip Antenna Devices. *J. Compo. Sci.* **2020**, *4*, 144.

40. Auric, P.; Van Dang, N.; Bandyopadhyay, A.; Zarzycki, J. Superparamagnetism and ferrimagnetism of the small particles of magnetite in a silicate matrix. *J. Non-Crystalline Solids* **1982**, *50*, 97–106, doi:10.1016/0022-3093(82)90203-4.
41. De Carvalho, J.; Medeiros, S.N.; Morales, M.; Dantas, A.L.; Carriço, A. Synthesis of magnetite nanoparticles by high energy ball milling. *Appl. Surf. Sci.* **2013**, *275*, 84–87, doi:10.1016/j.apsusc.2013.01.118.
42. Lu, T.; Wang, J.; Yin, J.; Wang, A.; Wang, X.; Zhang, T. Surfactant effects on the microstructures of Fe3O4 nanoparticles synthesized by microemulsion method. *Colloids Surfaces A Physicochem. Eng. Asp.* **2013**, *436*, 675–683, doi:10.1016/j.colsurfa.2013.08.00.
43. Kolen'Ko, Y.V.; Bañobre-López, M.; Rodríguez-Abreu, C.; Carbó-Argibay, E.; Sailsman, A.; Piñeiro-Redondo, Y.; Cerqueira, M.F.; Petrovykh, D.Y.; Kovnir, K.; Lebedev, O.I.; et al. Large-Scale Synthesis of Colloidal Fe3O4 Nanoparticles Exhibiting High Heating Efficiency in Magnetic Hyperthermia. *J. Phys. Chem. C* **2014**, *118*, 8691–8701, doi:10.1021/jp500816u.
44. Oliveira, M.A.D.; Yoshida, M.I.; Lima Gomes, E.C.D. Análise térmica aplicada a fármacos e formulações farmacêuticas na indústria farmacêutica. *Química Nova* **2011**, *34*, 1224–1230.
45. Williams, M. *The Merck Index: An Encyclopedia of Chemicals, Drugs, and Biologicals*, 15th Edition; O'Neil, M.J., Ed.; Royal Society of Chemistry: Cambridge, UK, 2013; Volume 74, pp. 339–339; ISBN 9781849736701.
46. Arayne, M.S.; Sultana, N.; Haroon, U.; Zaidi, B. In Vitro Evidences for Simvastatin and Losartan Potassium Interaction and its in vivo Implications. *J. Chil. Chem. Soc.* **2009**, *54*, 432–436, doi:10.4067/s0717-97072009000400024.
47. Goldberg, M.A.; Protsenko, P.; Smirnov, V.; Antonova, O.; Konovalov, A.; Vorckachev, K.; Kudryavtsev, E.; Barinov, S.; Komlev, V. The enhancement of hydroxyapatite thermal stability by Al doping. *J. Mater. Res. Technol.* **2020**, *9*, 76–88, doi:10.1016/j.jmrt.2019.10.032.
48. Fréty, R.; Santos, M.R.; Sales, R.F.; Silva, A.O.; Barbosa, C.B.M.; Pacheco, J.G. Flash Pyrolysis of Oleic Acid as a Model Compound Adsorbed on Supported Nickel Catalysts for Biofuel Production. *J. Braz. Chem. Soc.* **2014**, *25*, 2433–2443, doi:10.5935/0103-5053.2014027.